Journal of Materials Chemistry

Cite this: J. Mater. Chem., 2012, 22, 24439

www.rsc.org/materials

PAPER

Facile synthesis of nanostructured vanadium oxide as cathode materials for efficient Li-ion batteries

Yanyi Liu,[a] Evan Uchaker,[a] Nan Zhou,[ab] Jiangang Li,[ac] Qifeng Zhang[a] and Guozhong Cao*[a]

Received 23rd June 2012, Accepted 20th August 2012
DOI: 10.1039/c2jm34078j

Homogeneous VO_2 (B) nanorods approximately 100 nm in width and 1–2 μm in length have been fabricated *via* the hydrothermal process, and are then transformed into irregularly shaped V_2O_5 nanoparticles of several hundreds nanometers large and 20–30 nm thick after annealing the precursor material at 500 °C for 30 min. Both the V_2O_5 sheet-like nanoparticles and VO_2 (B) nanorods were tested as active cathode materials for Li-ion batteries. The V_2O_5 sheet-like nanoparticles delivered a high discharge capacity of 281 mA h g^{-1} at 50 mA g^{-1} and 191 mA h g^{-1} at 2400 mA g^{-1}; the material also demonstrated good cyclic stability with a small capacity loss of 35 mA h g^{-1} after 40 cycles. The VO_2 (B) nanorods and V_2O_5 sheet-like nanoparticles prepared by the straightforward, environmental friendly and high yield route investigated in this study could prove to be promising candidates for efficient Li-ion batteries.

Introduction

The expansion and demands for energy use in the past several decades are incomparable with any other documented era. These energy demands are driven by the development of powerful electronic devices such as thin, light-weight laptops and tablets and sustainable hybrid electric vehicles (HEV) and electric vehicles (EV).[1] Among all these innovations, energy and power supply have become one of the most essential issues that determine the successful adoption of the new technologies. Li-ion batteries, functioning as a key component of energy-storage, have been heralded for their combination of high energy density and power density, with good electrochemical reversibility and cyclic stability.[2] However, not only does the device technology become an important issue in order to further advance the Li-ion battery performance to satisfy the rapid growth of industrial needs, but the research and development on battery materials, especially nanomaterials for battery electrodes, has also been regarded equally essential.[3]

Nanomaterials for Li-ion battery electrodes have been extensively studied during the past decade due to their high Li^+ intercalation capability begotten from the large surface area electrode material in contact with the electrolyte. It has also been reported that the use of nanomaterials leads to the fast charge transfer kinetics and enhanced Li^+ diffusion in nanomaterials.[4] Moreover, nanomaterials can better accommodate large volume expansion and contraction during Li^+ intercalation and deintercalation, which could provide better mechanical integrity and cyclic stability.[4a,5]

With its high theoretical Li^+ intercalation capacity and feasible morphological control, various nanostructures of V_2O_5 and VO_2 (B) have been fabricated and investigated as promising candidates for Li-ion battery cathode materials. Common synthesis techniques of these materials include electrospun V_2O_5 nanofibers;[6] template-assisted drop cast V_2O_5 nanorods,[7] nanocable[8] and nanotube arrays;[9] polymer-assisted self-assembled hollow microspheres;[10] hydrothermal synthesis of VO_2 (B) nanobelts,[11,12] nanorods,[13] nanoflakes and nanoflowers.[14] Such synthesis techniques have produced materials with competitive Li^+ intercalation capacity, excellent rate capability and reversibility. However, the aforementioned studies utilized complex vanadium resource materials, long fabrication times and complicated processing methods, which in turn result in a high cost that limits the opportunities or large-scale industrial production.

This current research endeavour introduces a straightforward route involving environmental friendly raw materials and a simple fabrication process in preparing homogenous VO_2 (B) nanorods and V_2O_5 sheet-like nanoparticles. The V_2O_5 sheet-like nanoparticles demonstrate excellent rate capability and cyclic stability when tested as cathode materials for Li-ion batteries. The nanocrystallite formation mechanism, crystal phase, morphology, charge transfer kinetics and electrochemical properties were investigated.

Experimental section

The precursor solution was prepared using the same procedure as previously reported.[15] V_2O_5 powder (99.8%, Alfa-AESAR) was

[a]Department of Materials Science and Engineering, University of Washington, Seattle, WA 98195, USA. E-mail: gzcao@u.washington.edu
[b]College of Chemistry and Chemical Engineering, Central South University, Changsha, Hunan 410083, China
[c]Department of Applied Chemistry, Beijing Institute of Petrochemical Technology, Beijing 102617, China

added to de-ionized water and H_2O_2 (30 wt% in H_2O, Sigma-Aldrich) to form a solution with a V_2O_5 concentration (C_V) of 0.3 M and $n(H_2O_2) : n(V)$ of 8.05 : 1. The resulting solution was stirred and sonicated for 15 min, and then diluted to $C_V = 0.05$ M using de-ionized water. After sonicating the solution for 30 min, 2 ml of ethylene glycol (EG, VWR) was added as both a reducing agent and a surfactant. This solution was then left to stir overnight until the chemicals were homogeneously mixed.

The solution was then transferred into a Teflon lined stainless steel autoclave, where it was heated to 180 °C for 3 hours. A large amount of thin, dark blue flocculate precipitates were observed after the hydrothermal process. The resulting precipitates were collected and washed with de-ionized water and ethanol several times, and dried in air at 70 °C for 12 hours. A portion of the isolated precipitates were then rapidly ramped up to 500 °C in air, where the temperature was held for 30 min to form orthorhombic V_2O_5 sheet-like nanoparticles.

The crystal phase and crystallite size of the VO_2 (B) nanorods and V_2O_5 sheet-like nanoparticles after hydrothermal processing and subsequent heat treatment were studied using X-Ray Diffraction (XRD, Philips 1820 X-Ray Diffractometer) with Cu Kα radiation (0.15418 nm). The nanostructures were characterized by a scanning electron microscope (SEM, JEOL JSM-5200) and a transmission electron microscope (TEM, FEI Tecnai G2 F20) operated at 200 kV. The specific surface area and pore characteristics were determined by nitrogen sorption and absorption isotherms at 77 K (Quantachrome NOVA 4200e). Electrochemical impedance spectroscopy (EIS) was carried out on the V_2O_5 sheet-like nanoparticles after being discharged to different potentials using a Solartron 1287A equipped with a Solartron 1260 FRA/impedance analyzer at a selected frequency range from 100 kHz to 0.5 Hz.

The electrochemical properties of the hydrothermally synthesized VO_2 (B) nanorods and annealed V_2O_5 sheet-like nanoparticles were tested using 2032-type coin cells with metallic lithium as the counter and reference electrodes. The cathodes were prepared by mixing the active material, Super P carbon (TimCal), and PVDF in a weight ratio of 7 : 2 : 1. The electrolyte used was 1 M $LiPF_6$ in EC–DMC with a volume ratio of 1 : 1. The cyclic voltammetric (CV) curves were measured between 3.8 V and 1.6 V (*vs.* Li/Li^+) at a scan rate of 2 mV s^{-1}, and the lithium ion intercalation properties were investigated *via* the chronopotentiometric (CP) method using an Arbin BT-2000 battery tester operating at room temperature. The specific capacity values presented in this study were based on the weight of the active material alone.

Results and discussion

The XRD pattern of the hydrothermally synthesized product is shown in Fig. 1(a) and can be indexed to a monoclinic VO_2 (B) phase (space group: $C2/m$) with lattice parameters $a = 12.09$ Å, $b = 3.70$ Å, $c = 6.43$ Å and $\beta = 106.97°$ (JCPDS no. 81-2392). The color of the solution prior to and following hydrothermal treatment changed from orange to dark blue, respectively, indicating a change in the valency of the vanadium species from V^{5+} (V_2O_5) to V^{4+} (VO_2). The crystal structure of VO_2 (B) consists of edge-sharing VO_6 octahedral layers stacked along the c-direction of the unit cell.[14] It has been reported that ethylene glycol (EG)

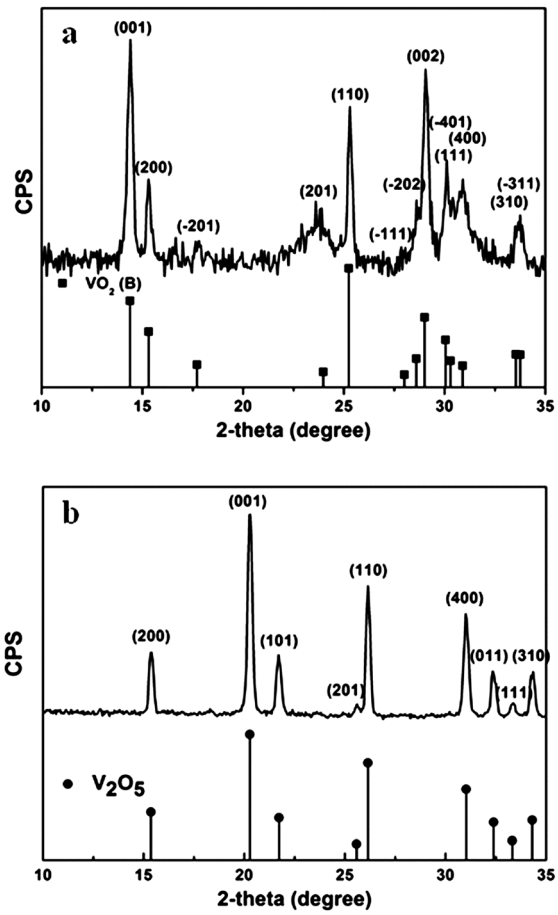

Fig. 1 X-Ray diffraction patterns of the (a) VO_2 (B) nanorods fabricated *via* the hydrothermal method and (b) V_2O_5 sheet-like nanoparticles after annealing at 500 °C in air.

can act as a reducing agent by inducing the oxidation process to form a carbonyl compound.[10,16] EG has also been a popular chemical reagent in the fabrication of oxide nanowires by serving as a ligand.[17] Moreover, EG can impede or suppress the hydrolysis of metal alkoxides due to the formation of linear polymers, which are usually expressed as $O–CH_2CH_2–O–M$.[18] In this study, EG served as both the reducing and surfactant agents that aided in the formation of the VO_2 (B) nanorods during the hydrothermal process.

The hydrothermally derived VO_2 (B) products were later annealed at 500 °C in an ambient environment, upon which the color of the powder turned bright yellow. Fig. 1(b) presents the XRD pattern of the powders annealed at 500 °C that shows the pure orthorhombic phase of V_2O_5. The crystallite size can be calculated using the Scherrer equation to be 27.8 nm from the (001) diffraction peak, and the lattice constants from the XRD pattern are calculated to be $a = 11.54$ Å, $b = 3.40$ Å, and $c = 4.37$ Å. These results agree well with the crystalline structure of the orthorhombic V_2O_5 (JCPDS no. 41-1426).

The SEM images of the products collected after the hydrothermal process and subsequent isolation are shown in Fig. 2(a) and (b). The SEM micrographs reveal the product to be uniform thin nanorods of approximately 100 nm in width and 1 μm in length. The successful one-step synthesis approach studied in this

research exploits a controllable route to fabricate the uniformly nanostructured VO_2 (B) without any heavy agglomerations.[13] The featured morphology of VO_2 (B) nanorods can also be observed from TEM images as shown in Fig. 2(c). Fig. 2(d) presents a high resolution TEM image with the indexed Fourier transform serving as a nanoscale selected area electron diffraction (SAED) pattern (Fig. 2(d) inset), clearly demonstrating the single crystalline nature of the VO_2 (B) nanorods. The image shows lattice fringes with an interspacing of 3.68 Å corresponding to the distance between two (010) crystal planes of the monoclinic VO_2 (B) (JCPDS no. 81-2392), indicating that the nanorods grew along the [010] direction.[12,19]

After annealing in air at 500 °C, the VO_2 (B) nanorods were transformed into fine V_2O_5 sheet-like nanoparticles approximately 200 nm in diameter and 20–30 nm thick as shown in the SEM and TEM images of Fig. 3(a)–(c). These sheet-like nanoparticles are uniformly distributed without heavy aggregation; however, there is some noticeable densification, due to Ostwald ripening effects, which could have been generated from the high temperature annealing process. The sheet-like morphology is not entirely homogeneous due to annealing related Ostwald ripening effects, but the confined thickness of the structure provides a short Li^+ diffusion path as well as a significant amount of pores and surface area which are beneficial for Li^+ intercalation.

The lattice fringe spacings of the V_2O_5 sheet-like nanoparticles are 3.50 Å and 4.39 Å as gathered from the HRTEM image in Fig. 3(d), and are consistent with the interplanar distances corresponding to the (201) and (001) planes, respectively. The well-resolved fringes confirm the localized single crystallinity of the V_2O_5 sheet-like nanoparticles, as further confirmed by the Fourier transform SAED pattern shown in the inset of Fig. 3(d).

V_2O_5 is the most stable vanadium complex, and can be formed by annealing less stable vanadium species to high temperature. The VO_2 (B) nanorods disassembled during the initial portion of the annealing process because of lattice mismatch and accompanying strain experienced during the transformation process.

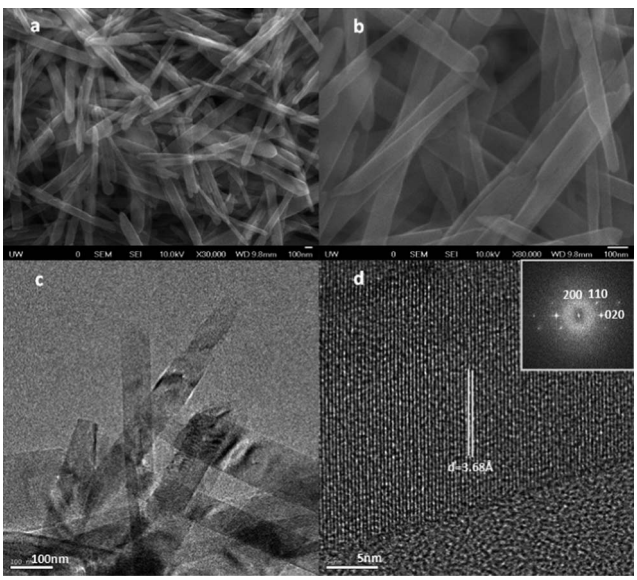

Fig. 2 SEM images (a and b) and TEM images (c and d) of the VO (B) nanorods directly synthesized from the hydrothermal process.

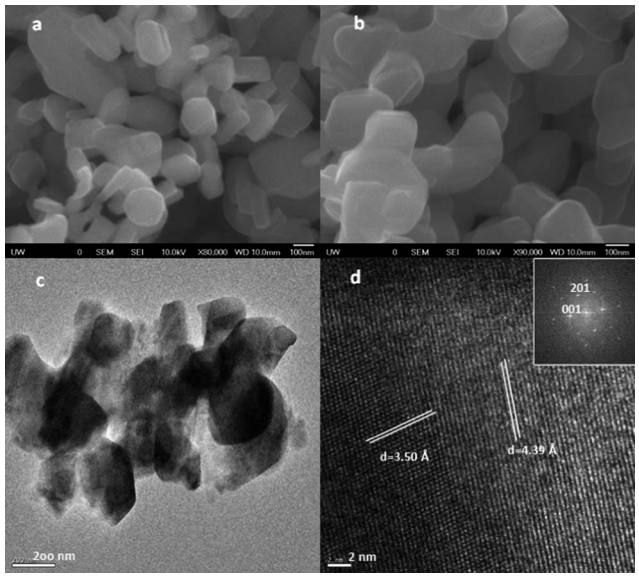

Fig. 3 SEM images (a and b) and TEM images (c and d) of the V_2O_5 sheet-like nanoparticles after annealing at 500 °C for 30 min.

This disassembly process yielded small V_2O_5 nanodiscs of approximately the same size as the initial VO_2 (B) nanorods (100 nm in diameter). Ostwald ripening and, a slight degree of, sintering then took place, producing the non-homogeneous V_2O_5 sheet-like nanoparticles that are approximately 200 nm in diameter and 20–30 nm thick.

Fig. 4(a) compares the typical nitrogen sorption isotherm of the VO_2 (B) nanorods and the V_2O_5 sheet-like nanoparticles. The multi-point Brunauer–Emmett–Teller (BET) surface areas are 31.0 $m^2 g^{-1}$ and 15.2 $m^2 g^{-1}$, respectively. The main precursor for the hydrothermal process is $V_2O_5 \cdot nH_2O$, with a crystal structure consisting of bilayered and slightly distorted VO_6 octahedra separated by crystalline water.

After hydrothermal synthesis, the crystal structure of the VO_2 (B) nanorods could be derived by dehydration of the crystalline water and linking of the oxygen atoms between the octahedral bilayers. This proposed formation process could explain the preservation of the one-dimensional nanorod morphology and the corresponding high surface area measured for the VO_2 (B) nanorods. Fig. 4(b) compares the nitrogen absorption isotherm of the VO_2 (B) nanorods and the V_2O_5 sheet-like nanoparticles. It is clear from the graph that the annealing step had little impact on the pore size and overall porosity of the sample, as the average pore sizes were 3.22 and 3.68 nm, respectively. The pore characteristics were conserved during the annealing process, thus any changes in the lithium ion intercalation performance could be attributed to the structural transformation to sheet-like nanoparticles. The beneficial intercalation capabilities of such morphologies have been documented in the literature.[27]

After thermal treatment at 500 °C in air for 30 min, the nanorods underwent drastic structural rearrangement to form the layered orthorhombic phase V_2O_5 sheet-like nanoparticles, with VO_5 pyramid shaped polyhedra propagating along the same plane. A decrease in the surface area after heat treatment in air has also been documented previously and was accounted for by the morphological, crystalline and structural stress evolutions

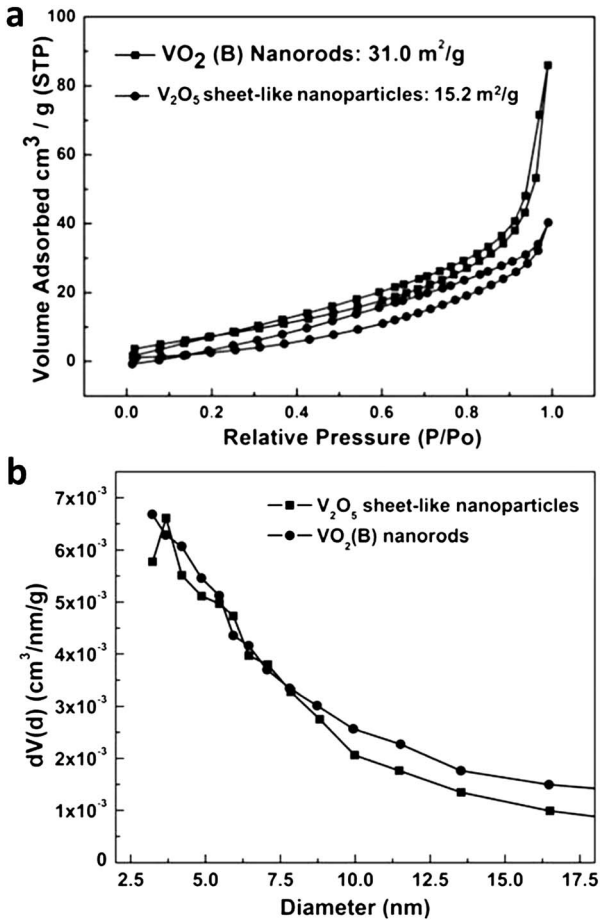

Fig. 4 Nitrogen (a) sorption and (b) absorption isotherms of the VO_2 (B) nanorods and V_2O_5 sheet-like nanoparticles.

induced by the annealing process.[20] The decrease in measured surface area could also be ascribed to the start of densification and grain coarsening effects, as seen in the SEM images.

Fig. 5 compares the VO_2 (B) nanorod and V_2O_5 sheet-like nanoparticle discharge curves during the first cycle when tested as cathode materials. The VO_2 (B) nanorods had an initial discharge capacity of 200 mA h g^{-1} at a current density of 50 mA g^{-1}, and a noticeably long intercalation plateau at around 2.5 V. This intercalation profile has been reported to be associated with the Li^+ insertion process into vanadium oxide and the reduction of the vanadium charge status (V^{4+}).[21] The discharge capacity of the V_2O_5 sheet-like nanoparticles for the first cycle is measured to be 264 mA h g^{-1} at a current density of 50 mA g^{-1}. This is very close to the theoretical intercalation capacity when two Li^+ ions are inserted into V_2O_5 (294 mA h g^{-1}). The insertion of three Li^+ ions per V_2O_5 formula unit should be avoided due to the formation of the irreversible ω-$Li_3V_2O_5$ phase. There are three distinct plateaus that could be observed in the discharge curve, indicating the following phase transitions from α-V_2O_5 to γ-V_2O_5: α–ε (~3.37 V), ε–δ (~3.18 V) and δ–γ (~2.31 V). The much improved Li^+ intercalation properties of the V_2O_5 sheet-like nanoparticles after heat treatment at 500 °C are attributed to the improved crystallinity and the fine crystallite size providing more open spaces as observed in the SEM and TEM images of Fig. 3(a)–(c).

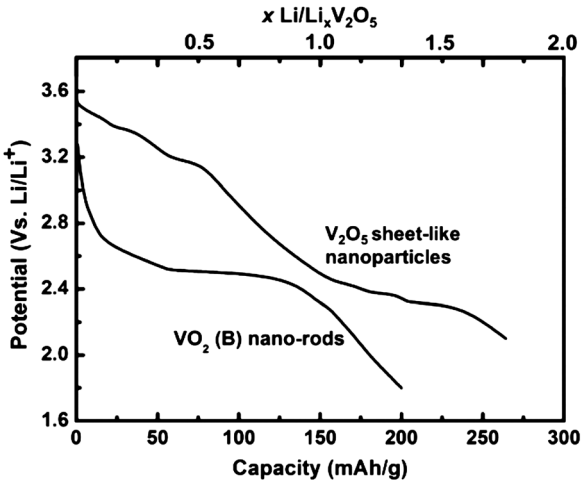

Fig. 5 The first cycle discharge curves of the VO_2 (B) nanorods and V_2O_5 sheet-like nanoparticles at 50 mA g^{-1}.

The discharge capacities of the VO_2 (B) nanorods and V_2O_5 sheet-like nanoparticles as cathode materials for Li-ion batteries are shown in Fig. 6(a) and (b). The discharge capacity for the VO_2 (B) nanorods initiates at 200 mA h g^{-1} under a current density of 50 mA g^{-1}, however it drastically drops to 146 mA h g^{-1} in the second cycle. At discharge rates higher than 150 mA g^{-1}, the discharge capacities were below 100 mA h g^{-1} starting at the 6th cycle. There could be two potential reasons for the poor

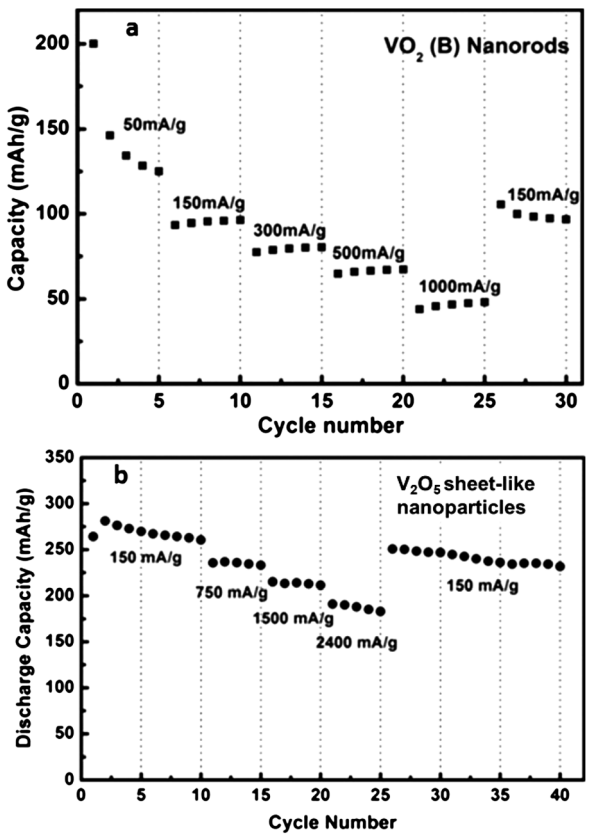

Fig. 6 Rate performances of the (a) VO_2 (B) nanorods and (b) V_2O_5 sheet-like nanoparticles as cathode materials at various current densities.

reversible electrochemical properties of the VO_2 (B) nanorods: (1) the large discharge–charge potential window of 3.8–1.8 V (*vs.* Li/Li^+) that could lead to the formation of irreversible phases; (2) the VO_2 nanorods could be heavily compacted during cycling, which is unfavorable for accommodating crystal and volume changes after intercalation–deintercalation.[14] These two factors could induce irreversible phase transitions during Li^+ intercalation–deintercalation, which devastate the efficient Li^+ diffusion channel and Li^+ intercalation sites in the crystal lattice and result in diminishing discharge capacity as well as poor rate performance.[22]

The electrochemical performance of the V_2O_5 sheet-like nanoparticles showed excellent Li^+ intercalation properties, including high discharge capacity, good rate capability and cyclic stability (Fig. 6(b)). The discharge capacity at 50 mA g^{-1} was 264 mA h g^{-1} for the 1st cycle, and increased to 281 mA h g^{-1} during the 2nd cycle. The measured discharge capacity was 267 mA h g^{-1}, 235 mA h g^{-1}, 215 mA h g^{-1}, and 191 mA h g^{-1} when cycled at current densities of 150 mA g^{-1}, 750 mA g^{-1}, 1500 mA g^{-1}, and 2400 mA g^{-1}, respectively. The capacity then rebound to 251 mA h g^{-1} at 150 mA g^{-1} in the 26th cycle, demonstrating the high degree of reversibility after cycling at higher current rates. After more than 15 cycles at 150 mA g^{-1}, the V_2O_5 sheet-like nanoparticles only experienced 19 mA h g^{-1} of discharge capacity loss. It is noteworthy that the discharge potential window chosen for the V_2O_5 sheet-like nanoparticles was 3.8–2.1 V (*vs.* Li/Li^+), and was chosen in order to avoid the formation of irreversible ω-$Li_3V_2O_5$ which could severely handicap the cycle stability.

The extraordinary electrochemical performance of the V_2O_5 sheet-like nanoparticles could be ascribed to the fine nanostructure of the well dispersed sheet-like nanoparticles and the amount of open spaces leading to good electrode–electrolyte contact which could lead to more intercalation sites during cycling. The 200 nm sheet-like nanoparticles that are 20–30 nm thick could also provide enhanced charge transfer kinetics at the electrode–electrolyte interface as well as a shortened Li^+ diffusion path in the electrode. These effects could explain the high discharge capacity under high current densities. Moreover the noticeable open spaces could lead to better accommodation of the volume change during Li^+ intercalation and deintercalation, therefore guaranteeing a better mechanical integrity and cyclic stability even after many cycles.

Fig. 7 compares the specific energy and power densities of the V_2O_5 sheet-like nanoparticles *versus* the electrodeposited porous V_2O_5 film electrode previously synthesized using the same precursor material.[23] The V_2O_5 sheet-like nanoparticles showed a high energy density of 790 W h kg^{-1} and 749 W h kg^{-1} when discharged slowly at 50 mA g^{-1} and 150 mA g^{-1}, respectively. A power density of 8.9 kW kg^{-1} could be achieved when discharged at 2.4 A g^{-1}, which is comparable to the high specific energy and power observed for the electrodeposited porous film electrodes.[23]

The cyclic voltammetry (CV) curves for the V_2O_5 sheet-like nanoparticles when cycled from 3.8–1.6 V (*vs.* Li/Li^+) are shown in Fig. 8. As previously reported in the literature, the formation of ω-$Li_3V_2O_5$ occurs, which can be designated by the missing anodic peaks corresponding to the ε–α, δ–ε and γ–δ phase transitions after the first cathodic scan.[15,24] After 10 cycles, the area covered by the CV curve is noticeably reduced and

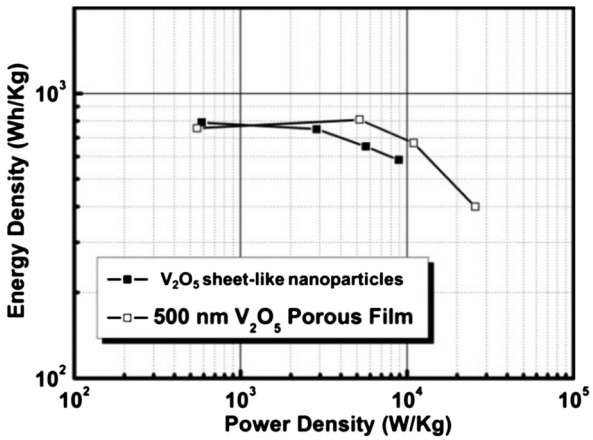

Fig. 7 The Ragone plots comparing the power density and energy density of ~500 nm porous V_2O_5 film cathodes and the V_2O_5 sheet-like nanoparticles.

the cathodic and anodic peaks have degraded considerably. The electrochemical degradation can also be reflected in the rate capability test as shown in Fig. 9, when the material was discharged to 1.8 V (*vs.* Li/Li^+). The initial discharge capacity of the V_2O_5 sheet-like nanoparticles was 398 mA h g^{-1} at 50 mA g^{-1}, but drastically dropped to 319 mA h g^{-1} with subsequent cycling.

This capacity drop can be attributed to the potential irreversible phase formation of ω-$Li_3V_2O_5$ at higher discharge rate. Following this, the discharge capacities were 272 mA h g^{-1}, 218 mA h g^{-1}, 148 mA h g^{-1}, and 84 mA h g^{-1} at current densities of 150 mA g^{-1}, 750 mA g^{-1}, 1500 mA g^{-1}, and 2400 mA g^{-1}, respectively. The capacity then rebound to 212 mA h g^{-1} when cycled at 150 mA g^{-1} in the 26th cycle. The discharge capacity of ω-$Li_3V_2O_5$ at higher current densities, *i.e.* 1500 mA g^{-1} or 2400 mA g^{-1}, was considerably lower when compared to γ-$Li_3V_2O_5$ as shown in Fig. 5(b), indicating that the Li^+ intercalation kinetics in ω-$Li_3V_2O_5$ were poorer than that in γ-$Li_3V_2O_5$.

In order to better understand the mechanism behind these phenomena, EIS was carried out on the same coin cell (containing V_2O_5 sheet-like nanoparticles) when discharged to 2.0 V, 1.8 V and 1.6 V (*vs.* Li/Li^+) in order to directly observe the

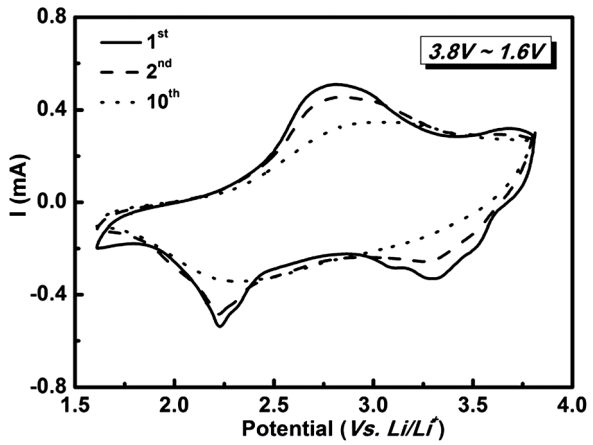

Fig. 8 The cyclic voltammograms of the V_2O_5 sheet-like nanoparticles within the voltage range of 3.8–1.6 V (*vs.* Li/Li^+) for the 1st, 2nd and 10th cycles.

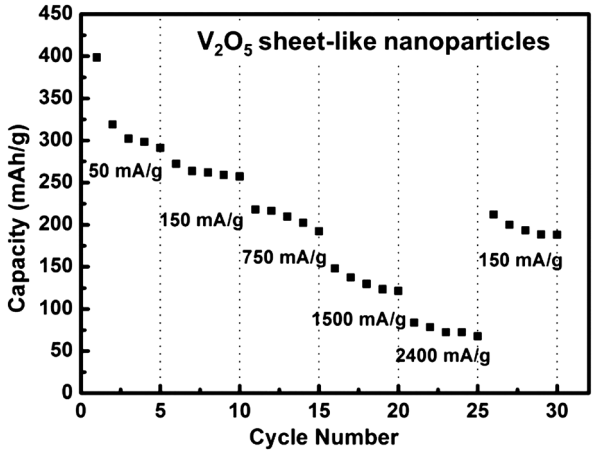

Fig. 9 Rate performances of the V_2O_5 sheet-like nanoparticles as cathode materials when discharged to 1.8 V (*vs.* Li/Li^+) at various current densities.

different Li^+ intercalation content and phase transitions. The typical Nyquist plots as gathered within the frequency range of 100 kHz–0.5 Hz are shown in Fig. 10(a), and display two well-defined regions: a depressed semicircle in the high-frequency region and a sloped line in the low-frequency region. These two regions correspond to the charge transfer reactions at the electrode–electrolyte interface and Warburg impedance associated with Li^+ diffusion in the cathode materials, respectively.[25]

Fig. 10 also shows a simple equivalent circuit which can be applied to simulate the impedance spectra.[25c] In the equivalent circuit, R_s represents the electrolyte resistance, which could also be verified by the ionic conductivity of the liquid electrolyte, the electrode area and the distance between the working electrode and the counter electrode; R_{ct} stands for charge transfer resistance between the electrode and the electrolyte; CPE is the double layer capacitance on the electrode surface; and W is the Warburg impedance. A well-fitting agreement could be obtained using the equivalent circuit, as shown between the dots (experimental data) and the lines (fitting results from the equivalent

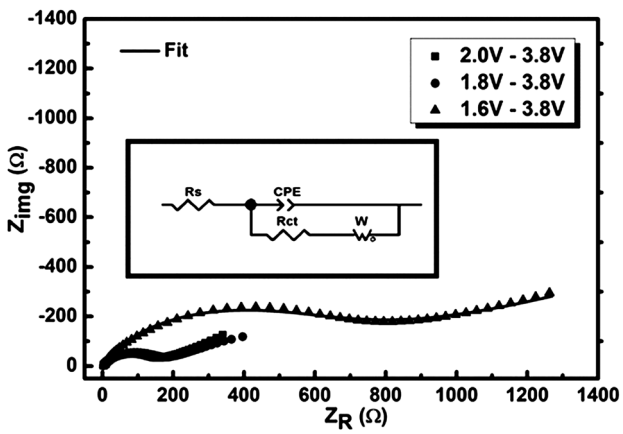

Fig. 10 The Nyquist plots of the coin cell with the V_2O_5 sheet-like nanoparticles as cathode materials discharged to 2.0 V, 1.8 V and 1.6 V, respectively (dots: experimental data; lines: fitting results) and the equivalent circuit used to fit the impedance data.

Table 1 The simulated electrolyte and charge transfer resistance from Fig. 10

	3.8–2.0 V	3.8–1.8 V	3.8–1.6 V
$R_{electrolyte}$ (Ω)	2.1	2.1	2.9
$R_{charge\ transfer}$ (Ω)	131.9	145.4	181.9

circuit) in Fig. 10. The simulated results are listed in Table 1, where it can be observed that the charge transfer resistances increased when the sample was discharged to lower voltages, which is indicative of poorer charge transfer kinetics at the electrode–electrolyte interface when ω-$Li_3V_2O_5$ is potentially formed.

The charge transfer resistance is 181.9 Ω when the coin cell was discharged to 1.6 V, which is larger than 131.9 Ω at 2.0 V and 145.4 Ω at 1.8 V. This observation could sufficiently explain the reason for the poor rate performance of the coin cell when discharged to 1.8 V (*vs.* Li/Li^+) with the V_2O_5 sheet-like nanoparticles as cathode materials (Fig. 9). This result is consistent with the previous data reported in the literature.[25a,26]

Conclusions

VO_2 (B) nanorods were successfully synthesized using an ethylene glycol (EG) aided hydrothermal process. EG acted as reducing and surfactant agents, which aided in the formation of VO_2 (B) with one-dimensional nanorod morphology. After annealing at 500 °C in air for 30 min, uniform V_2O_5 sheet-like nanoparticles with a diameter of 200 nm and a thickness of 20–30 nm were formed. The V_2O_5 sheet-like nanoparticles exhibited excellent electrochemical properties when tested as a cathode material for Li-ion batteries. The high discharge capacity, rate capability and good cyclic stability could be ascribed to: (1) the sufficient contact between electrode materials and the electrolyte providing more intercalation sites due to the large amount of pores and spaces between the sheet-like nanoparticles; (2) a short Li^+ diffusion path and improved charge transfer kinetics in the sheet-like nanoparticles; and (3) considerable flexibility in the nanostructure which could maintain its mechanical integrity by accommodating cycling related volume changes, thereby leading to excellent cell reversibility. The V_2O_5 sheet-like nanoparticles could prove to be a promising cathode material candidate due to outstanding electrochemical performance combined with the simple and controllable fabrication method.

Acknowledgements

This research work has been financially supported in part by National Science Foundation (CMMI-1030048) and Pacific Northwest National Laboratory (PNNL). Part of this work was conducted at the University of Washington NanoTech User Facility, a member of the NSF National Nanotechnology Infrastructure Network (NNIN).

References

1 N. Armaroli and V. Balzani, *Angew. Chem., Int. Ed.*, 2007, **46**, 52–66.
2 (*a*) J. M. Tarascon and M. Armand, *Nature*, 2001, **414**, 359; (*b*) M. Armand and J. M. Tarascon, *Nature*, 2008, **451**, 652–657.

3 J. Maier, *Nat. Mater.*, 2005, **4**, 805–815.
4 (*a*) J. Liu, G. Z. Cao, Z. G. Yang, D. H. Wang, D. Dubois, X. D. Zhou, G. L. Graff, L. R. Pederson and J. G. Zhang, *ChemSusChem*, 2008, **1**, 676–697; (*b*) D. Liu and G. Cao, *Energy Environ. Sci.*, 2010, **3**, 1218–1237; (*c*) Y. Wang and G. Z. Cao, *Adv. Mater.*, 2008, **20**, 2251–2269; (*d*) C.-j. Liu, U. Burghaus, F. Besenbacher and Z. L. Wang, *ACS Nano*, 2010, **4**, 5517–5526.
5 (*a*) C. Jiang, E. Hosono and H. Zhou, *Nano Today*, 2006, **1**, 28–33; (*b*) Y. G. Guo, J. S. Hu and L. J. Wan, *Adv. Mater.*, 2008, **20**, 2878–2887; (*c*) P. G. Bruce, B. Scrosati and J.-M. Tarascon, *Angew. Chem., Int. Ed.*, 2008, **47**, 2930–2946.
6 L. Mai, L. Xu, C. Han, X. Xu, Y. Luo, S. Zhao and Y. Zhao, *Nano Lett.*, 2010, **10**, 4750–4755.
7 K. Takahashi, S. J. Limmer, Y. Wang and G. Z. Cao, *J. Phys. Chem. B*, 2004, **108**, 9795–9800.
8 K. Takahashi, Y. Wang and G. Z. Cao, *J. Phys. Chem. B*, 2005, **109**, 48–51.
9 Y. Wang, K. Takahashi, H. M. Shang and G. Z. Cao, *J. Phys. Chem. B*, 2005, **109**, 3085–3088.
10 A. M. Cao, J. S. Hu, H. P. Liang and L. J. Wan, *Angew. Chem., Int. Ed.*, 2005, **44**, 4391–4395.
11 F. Sediri and N. Gharbi, *Mater. Lett.*, 2009, **63**, 15–18.
12 K.-F. Zhang, S.-J. Bao, X. Liu, J. Shi, Z.-X. Su and H.-L. Li, *Mater. Res. Bull.*, 2006, **41**, 1985–1989.
13 S. A. Corr, M. Grossman, Y. Shi, K. R. Heier, G. D. Stucky and R. Seshadri, *J. Mater. Chem.*, 2009, **19**, 4362–4367.
14 J. Ni, W. Jiang, K. Yu, Y. Gao and Z. Zhu, *Electrochim. Acta*, 2011, **56**, 2122–2126.
15 Y. Y. Liu, M. Clark, Q. F. Zhang, D. M. Yu, D. W. Liu, J. Liu and G. Z. Cao, *Adv. Energy Mater.*, 2011, **1**, 194–202.
16 (*a*) F. Kim, S. Connor, H. Song, T. Kuykendall and P. Yang, *Angew. Chem., Int. Ed.*, 2004, **116**, 3759–3763; (*b*) X. Chen, *et al.*, *Nanotechnology*, 2004, **15**, 1685.
17 X. Jiang, Y. Wang, T. Herricks and Y. Xia, *J. Mater. Chem.*, 2004, **14**, 695–703.
18 (*a*) M. Benaissa, C. Pham-Huu, J. Werckmann, C. Crouzet and M. J. Ledoux, *Catal. Today*, 1995, **23**, 283–298; (*b*) G. Korb, G. Levy, M. Brini and A. Deluzarche, *J. Organomet. Chem.*, 1970, **23**, 437–443; (*c*) D. E. Fenton, R. R. Gould, P. G. Harrison, T. B. Harvey Iii, G. M. Omietanski, K. C. T. Sze and J. J. Zuckerman, *Inorg. Chim. Acta*, 1970, **4**, 235–243.
19 M. Li, F. Kong, Y. Zhang and G. Li, *CrystEngComm*, 2011, **13**, 2204–2207.
20 H. Li, P. He, Y. Wang, E. Hosono and H. Zhou, *J. Mater. Chem.*, 2011, **21**, 10999–11009.
21 (*a*) H. Li, T. Zhai, P. He, Y. Wang, E. Hosono and H. Zhou, *J. Mater. Chem.*, 2011, **21**, 1780–1787; (*b*) T. Chirayil, P. Y. Zavalij and M. S. Whittingham, *Chem. Mater.*, 1998, **10**, 2629–2640.
22 C. M. Ban, N. A. Chernova and M. S. Whittingham, *Electrochem. Commun.*, 2009, **11**, 522–525.
23 Y. Liu, J. Li, Q. Zhang, N. Zhou, E. Uchaker and G. Cao, *Electrochem. Commun.*, 2011, **13**, 1276–1279.
24 C. Delmas, H. Cognac-Auradou, J. M. Cocciantelli, M. Ménétrier and J. P. Doumerc, *Solid State Ionics*, 1994, **69**, 257–264.
25 (*a*) C. Leger, S. Bach, P. Soudan and J. P. Pereira-Ramos, *J. Electrochem. Soc.*, 2005, **152**, A236–A241; (*b*) V. Vivier, J. Farcy and J.-P. Pereira-Ramos, *Electrochim. Acta*, 1998, **44**, 831–839; (*c*) C.-J. Cui, G.-M. Wu, H.-Y. Yang, S.-F. She, J. Shen, B. Zhou and Z.-H. Zhang, *Electrochim. Acta*, 2010, **55**, 8870–8875.
26 S.-I. Pyun and J.-S. Bae, *J. Power Sources*, 1997, **68**, 669–673.
27 N. Zhou, Y. Y. Liu, J. Li, E. Uchaker, S. Liu, K. Huang and G. Z. Cao, *J. Power Sources*, 2012, **213**, 100–105.